

# Sustainable 3D Printing of Recyclable Biocomposite Empowered by Flash Graphene

Yuchao Wu, Paul A. Advincula, Oliver Giraldo-Londoño, Yukai Yu, Yunchao Xie, Zhenru Chen, Guoliang Huang, James M. Tour,\* and Jian Lin\*



Cite This: <https://doi.org/10.1021/acsnano.2c08157>



Read Online

ACCESS |



Metrics & More



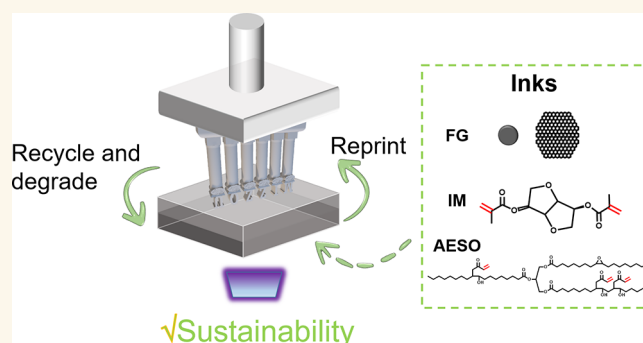
Article Recommendations



Supporting Information

**ABSTRACT:** Sustainability of 3D printing can be reflected in three main aspects: deployment of renewable inks, recycling of printed products, and applications for energy- and materials-savings. In this work, we demonstrated sustainable vat-photopolymerization (VPP)-based 3D printing in a whole life-cycle process by developing a renewable ink made of soybean oil and natural polyphenols and recycling the ink for reprinting or converting printed biocomposite to flash graphene (FG) as reinforcing nanofillers in the biocomposite. We also realized its applications in fabricating lightweight, materials-saving 3D structures, acoustic metamaterials, and disposable micro-reactors for time-saving and efficiency-improving synthesis of metal–organic framework nanostructures. In addition to enhancing the tensile strength and Young's modulus of the biopolymers by 42% and 232% with only 0.6 wt % FG nanofillers, respectively, FG improved the printability of the ink in forming 3D tubular structures, which are usually very hard to be achieved in transparent resin. Success of this work will inspire further development for sustainability in 3D printing.

**KEYWORDS:** 3D printing, biocomposite, flash graphene, recyclable, sustainability



Additive manufacturing, also known as 3D printing, is a rapid prototyping technique that builds objects in a layer-by-layer manner.<sup>1,2</sup> It offers advantages of high design freedom, efficient product development, and customized part production from a wide range of raw materials including metals, ceramics, and polymers,<sup>3,4</sup> thus making it a promising manufacturing form. The trend of sustainable development in society calls for sustainability in 3D printing, which is expected to further exploit the potential. Sanchez-Rexach et al. proposed four key elements to address sustainability in 3D printing: (1) development of hardware and processes that minimize waste generation; (2) deployment of renewable raw materials; (3) reuse and recycling of printed products; and (4) applications in sustainability.<sup>5</sup> Among them, development of the renewable inks for printing high-performance 3D structures that are recyclable is a grand challenge. Among the various types of 3D-printable inks, photoactive acrylates are the most widely used ones for the vat-photopolymerization (VPP)-based 3D printing techniques, e.g., digital light processing and liquid crystal display (LCD).<sup>6</sup> They share more than half of the photoreactive market due to their high photoreactivity, printability, and good mechanical and thermal properties of the printed objects.<sup>2</sup> But they are usually synthesized from petroleum-based chemicals, which are

not renewable, therefore increasing demand on petroleum resources.<sup>7</sup>

Biomass precursors, e.g., soybean oil and natural polyphenols, are degradable and renewable for producing sustainable materials because of their abundance and low cost.<sup>8</sup> The structures of soybean oil are very simple and mainly composed of triglycerides, while their unsaturated double bonds are located inside the fatty acid chain, leading to low photoreactivity. To improve its photoreactivity, it can be modified to acrylated epoxidized soybean oil (AESO).<sup>9</sup> But the resulting plastics lack competitive mechanical properties compared with some engineering polymers possibly due to the long fatty acid chain.<sup>10,11</sup> On the other hand, VPP-based 3D printing of tubular structures has shown potential applications in cell separation and nanomaterial synthesis owing to the high printing resolution of VPP-based printing

**Received:** August 15, 2022

**Accepted:** September 26, 2022



ACS Publications

© XXXX American Chemical Society

A

<https://doi.org/10.1021/acsnano.2c08157>  
ACS Nano XXXX, XXX, XXX–XXX

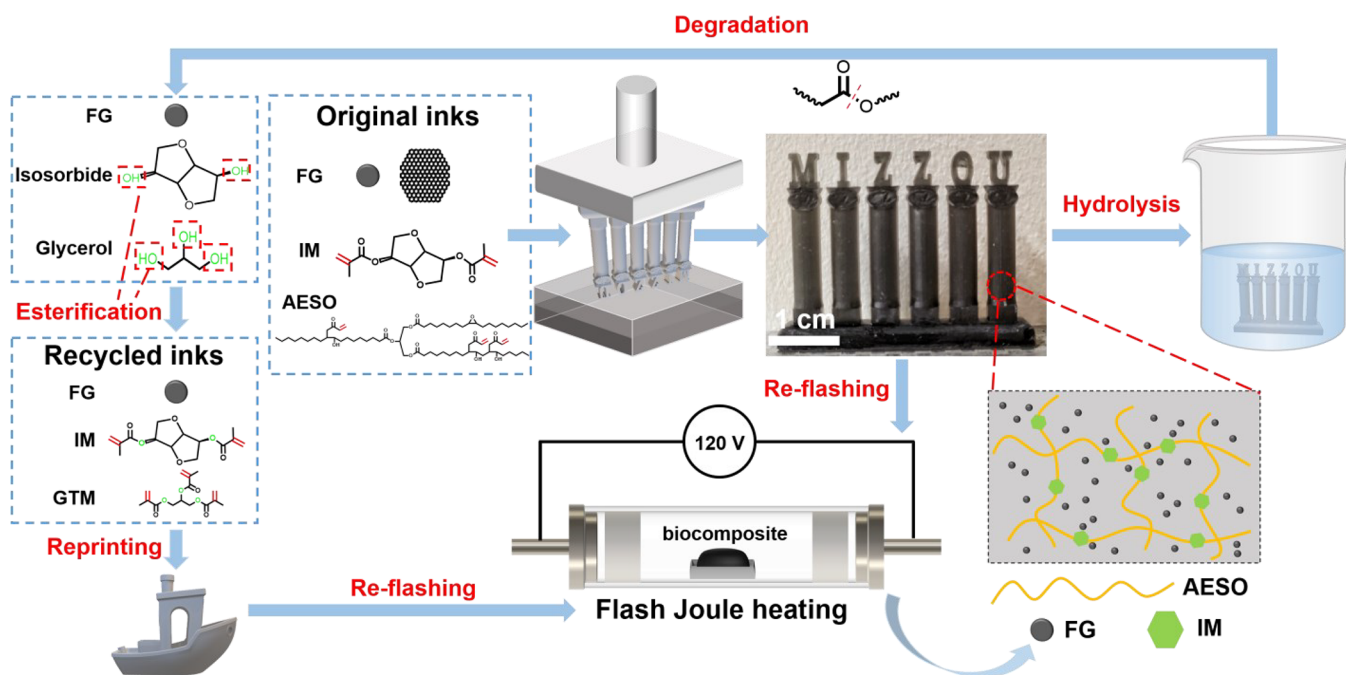


Figure 1. Scheme showing workflow of printing, reprocessing, and recycling of the biocomposite. FG: flash graphene; IM: isosorbide methacrylate; AESO: acrylated epoxidized soybean oil; GTM: glyceryl trimethacrylate.

techniques.<sup>12,13</sup> But the light penetration depth in a transparent resin is relatively large. When using it for printing the 3D tubular structures with sub-millimeter channels, the residual resin in the channels may be over-cured, resulting in channel blockage. Thus, 3D printing of the tubular structures remains a challenge.<sup>14,15</sup> The mostly transparent AESO resin also has this issue, while to our best knowledge it has not been solved. Thus, to tackle the issues, a type of nanofillers that can act as the reinforcing nanofillers to enhance the mechanical performance while acting as a light absorber to prevent over-curing in printing the 3D tubular structures is highly demanded.

Flash graphene (FG) is produced by a flash Joule heating (FJH) process from various types of carbon sources including mixed waste plastics.<sup>16–18</sup> As a type of graphitic material, it possesses high surface area and offers enhanced interfaces to strengthen the mechanical properties of host materials, e.g., asphalt and synthetic polymers.<sup>16–19</sup> In addition, FG can efficiently absorb light including UV, thus showing potential of preventing over-curing for the underlying layers. Indeed, there are some light absorbers on the market, such as food coloring, but they usually do not have the role of enhancing the mechanical properties. Herein, FG has the dual functions of enhancing the mechanical properties and acting as a light absorber. Despite these potential benefits, FG has not been demonstrated for application in 3D printing of biocomposite objects with high-precision, complex, and hollow structures with improved mechanical performance. Herein, we report sustainable 3D printing of an FG/soybean oil-based biocomposite for applications in a lightweight structure, a material-saving acoustic metastructure, and a time-saving, efficiency-improved, disposable microfluidic reactor. Advances of this work in the field can be summarized as follows. First, FG was employed in the ink to improve both the mechanical property of the biopolymers and the printability of the ink in forming 3D tubular microstructures. Second, the ink is

renewable and biocomposite is degradable. The printed parts can be recycled to the ink for reprinting or be upgraded to FG by the FJH process at the end of their service, as the source of carbon in the biomass is from CO<sub>2</sub>, which is eventually fixed as solid FG without re-entering the carbon cycle. Third, the printed 3D structures show materials-saving characteristics in load-bearing and sound-attenuation applications. The printed microfluidic reactors save time and improve the efficiency in nanomaterials synthesis. In summary, from the aspects of ink renewability, product recyclability, and sustainable applications, an important progression toward sustainable 3D printing is made.

## RESULTS AND DISCUSSION

**Performance of 3D-Printed Biocomposite.** The workflow showing the sustainable 3D printing process is illustrated in Figure 1. The process starts with printing objects from an original ink consisting of AESO, isosorbide methacrylate (IM), and FG. The main structure of AESO is the triglyceride with many soft fatty acid chains. IM has aromatic rings, which would provide rigidity to strengthen the mechanical property when it participates in cross-linking the AESO structures.<sup>20,21</sup> Therefore, we synthesized IM by modifying a natural polyphenol of isosorbide, one of the top 12 most promising renewable building blocks (Figure S1).<sup>22</sup> It was used as a comonomer of AESO in the photoresin. Upon UV irradiation from the VPP printer, the double bonds in IM and AESO are initiated to form a cross-linked IM/AESO network biopolymer (Figure 1). The FG is well-dispersed in the ink and acts as a reinforcing nanofiller in the printed biocomposite. The printed objects show a high printing resolution (Figure S2). They can be finally degraded to FG, isosorbide, and glycerol through hydrolysis. Through an esterification reaction, the hydrolysis products, i.e., isosorbide and glycerol, can be modified to IM and glyceryl trimethacrylate (GTM) with double bonds, respectively. This recycled ink can be used for reprinting 3D

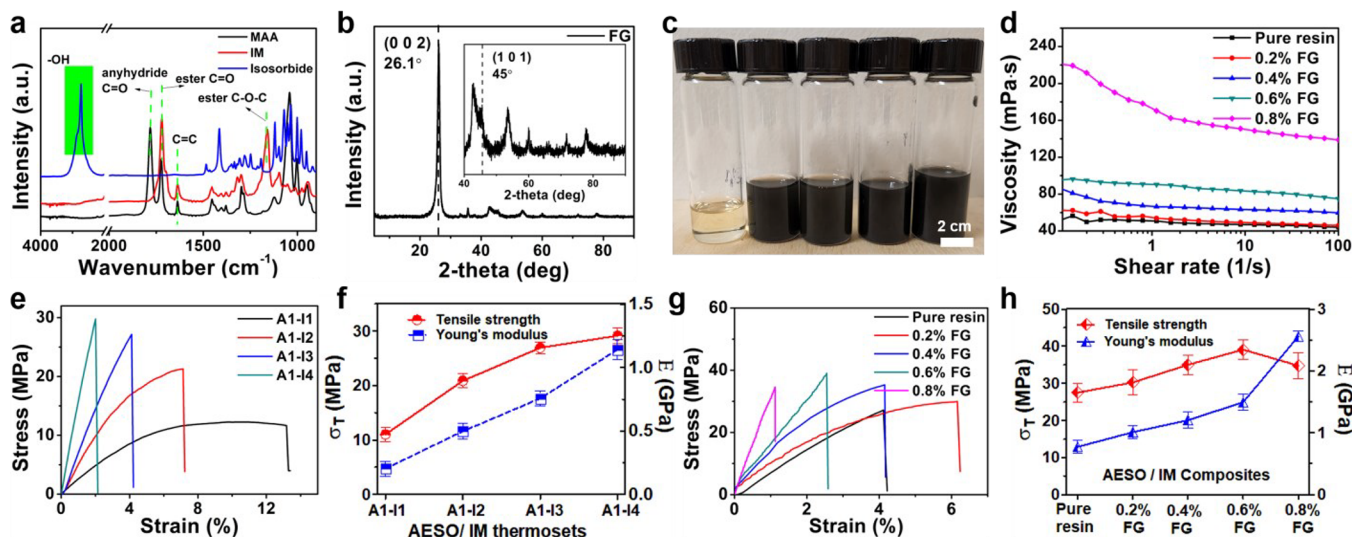


**Figure 2.** (a) FTIR spectra of IM, MAA, and isosorbide. (b) An XRD spectrum of FG. (c) A photograph of a pure AESO/IM resin and AESO/IM/FG resins with FG weight ratios ranging from 0.2 wt % to 0.8 wt %. (d) Viscosity–shear rate curves of the AESO/IM/FG resins with different FG weight ratios. (e) Stress–strain curves of the pure AESO/IM biopolymers with AESO-to-IM molar ratios of 1:1 (A1-I1), 1:2 (A1-I2), 1:3 (A1-I3), and 1:4 (A1-I4). (f) Tensile strength ( $\sigma_T$ ) and Young's modulus ( $E$ ) of biopolymers. (g) Stress–strain curves and (h) tensile strength ( $\sigma_T$ ) and Young's modulus ( $E$ ) of the biocomposite with varied FG weight ratios ranging from 0.2 to 0.8 wt %.

objects. Or the printed 3D objects can be flashed to FG by the FJH process once they reach the end of service.

Figure 2 shows the characterization of the ink precursors and mechanical performance of the printed objects. As shown in Figure 2a, the peak of the hydroxyl groups clearly appears in the Fourier transform infrared (FTIR) spectrum of isosorbide, while these hydroxyl peaks disappear, and the peaks of the carbon–carbon double bonds appear in the IM FTIR spectrum after the isosorbide is modified with methacrylic anhydride (MAA) by an esterification reaction. The anhydride ester C=O bond disappears in the IM spectrum, suggesting that MAA is not traceable in synthesized IM. In addition to strengthening the AESO network as shown in the following, IM can be used as a diluent to effectively reduce ink viscosity (Figure S3), thus facilitating the VPP-based 3D printing.<sup>23</sup> The FG was made from the metallurgical coke with a 97% FG yield and >95% process yield and was selected as the additive to the resin. Here, FG yield denotes the percentage of Raman spectra that could be characterized as graphene (Figure S4). To meet this criterion, the Raman spectrum must show (1) a minimum  $I_{2D}/I_G$  ratio of  $\geq 0.3$ , (2) a signal-to-noise ratio of  $>5$  in the 2D band region, and (3) a 2D band with an fwhm of  $<100$   $\text{cm}^{-1}$ . Process yield denotes the mass of the product of the FJH process divided by the mass of the feedstocks. This result is further suggested by X-ray diffraction (XRD) showing profound peaks of (002) and (101) at  $26.1^\circ$  and  $45^\circ$ , respectively (Figure 2b). The purity of FG was high, as determined by the X-ray photoelectron spectroscopy. There are no observable impurity peaks in the low-resolution spectra of the samples (Figure S5). Transmission electron microscopy (TEM) images show that FG has sizes of hundreds of nanometers and wrinkled structures (Figure S6).

FG exhibits very good dispersion in the resin (Figure 2c), which is beneficial to form uniformly distributed FG in the printed solid objects. All of the prepared resin with FG weight ratios of up to 0.8% has a viscosity of  $<1.3$  Pa·s at room temperature (Figure 2d and Figure S3), showing that it meets the requirement for VPP.<sup>23</sup> To validate the hypothesis that the

rigid aromatic rings in IM would enhance the mechanical properties, we varied the molar ratios of IM in the pure AESO/IM resin. Figure 2e,f show that the tensile strength ( $\sigma_T$ ) and Young's modulus ( $E$ ) increase from 11.03 to 29.17 MPa and 0.20 and 1.14 GPa, respectively, when the AESO-to-IM molar ratio in the AESO/IM resin varies from 1:1 (A1-I1) to 1:4 (A1-I4). The increment of  $\sigma_T$  is 89.3%, 29.0%, and 8.3%, respectively, for the increased mole ratio of IM in the resin (Table S2), while the biomass content decreases from ~62.8% to ~50.8%. Thus, by balancing the strengthening effect and biomass content, A1-I3 resin is selected as the model material for all the following experiments. When FG is composited with the AESO/IM resin, both the tensile strength and Young's modulus of the printed biocomposite increase. Figure 2g,h show that the tensile strength of the AESO/IM/FG biocomposite reaches the maximum value when 0.6 wt % FG is added, averagely increasing by 42% compared to the printed object from the pure A1-I3 resin. The Young's modulus is enhanced by 232%, from 0.77 GPa to 2.56 GPa, when FG is 0.8 wt %.

**3D-Printed Lightweight Biocomposite Structures for Material-Saving Applications.** A goal in the engineering design of mechanical components is to distribute materials in an efficient manner so that performance is maximized while cost is minimized. Traditionally, human intuition and analytical methods have steered mechanical design, potentially leading to suboptimal components due to the limited design freedom that can be achieved this way. Recently, computational design approaches have been used to aid designers in achieving optimized designs that often outperform those obtained via human intuition. Introduced in the late 1980s, topology optimization is a computational design approach that seeks to find an optimized material distribution while satisfying specified design constraints.<sup>24</sup> One of the most important design problems in topology optimization aims to minimize the structural mass while satisfying constraints imposed on mechanical stresses to ensure that the optimized structures carry the applied loads without experiencing local materials



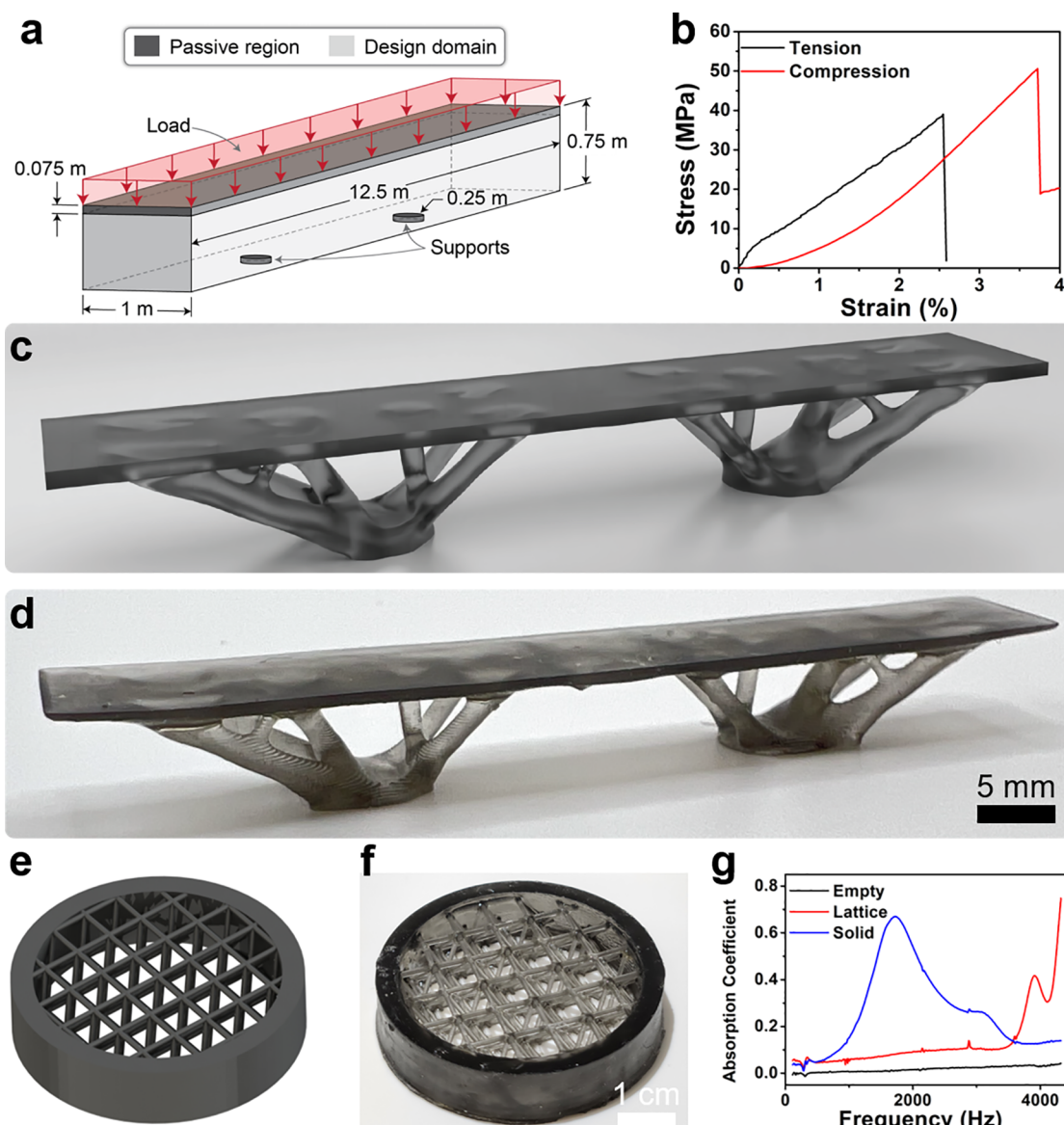


**Figure 3.** (a) Design domain and boundary conditions of a topology-optimized structure for roof support inspired by QNCC. The dark gray portion is a passive (nondesignable) region that represents the roof to be supported, while the light gray portion is the design domain where the optimized structure will be designed. (b) Tensile and compressive stress–strain curves used to determine an equivalent Young’s modulus and tensile and compressive yield strength. (c) A rendered 3D model by the optimization algorithm. (d) Photograph of the rendered 3D model biocomposite structure. (e) A rendered acoustic 3D metastructure model. (f) Photograph of the 3D-printed metastructure. (g) Acoustic absorption of empty, lattice, and solid structure. Objects shown in d and f were printed from inks made of A1-I3 and 0.6 wt % FG.

failure. Here, we show that the 3D-printed biocomposite can be used for such a purpose.

First, we adopted the unified stress constraints formulated by Giraldo-Londoño and Paulino with model parameters tailored to the Drucker-Prager failure function to design a roof support structure inspired by the Qatar National Convention Center (QNCC).<sup>25,26</sup> Here, we aim to design a structure whose dimensions are approximately one-tenth of those of the original QNCC (Figure 3a). As shown in the figure, a passive region is considered to represent the roof of the structure (i.e., a nondesignable domain). Vertical loads are applied to the top of the domain to represent gravity loads from the roof. Moreover, two circular supports equidistant from the center of the domain are used to transmit the loads to the ground. The mechanical behavior used for the modeling is the one of the AESO/IM/FG biocomposite developed in this study. Its

stress–strain behaviors under tension and compression are shown in Figure 3b, where the Young’s modulus and tensile and compressive yield stresses are obtained for the modeling. Although the stress–strain curves show a nonlinear behavior, for simplicity, we modeled the material as a linear elastic material with a Young’s modulus obtained from the linear portion of the curves in Figure 3b. A rendering of the optimized design obtained by the optimization algorithm is depicted in Figure 3c, which displays a tree-like feature. The optimized design was then 3D printed using the developed biocomposite, as illustrated in Figure 3d. The structure displayed herein showcases the use of topology optimization for the sustainable design of strong, lightweight structures with reduced use of raw materials.

In addition, thanks to the printability of the biocomposite, we can customize an acoustic metastructure with a special



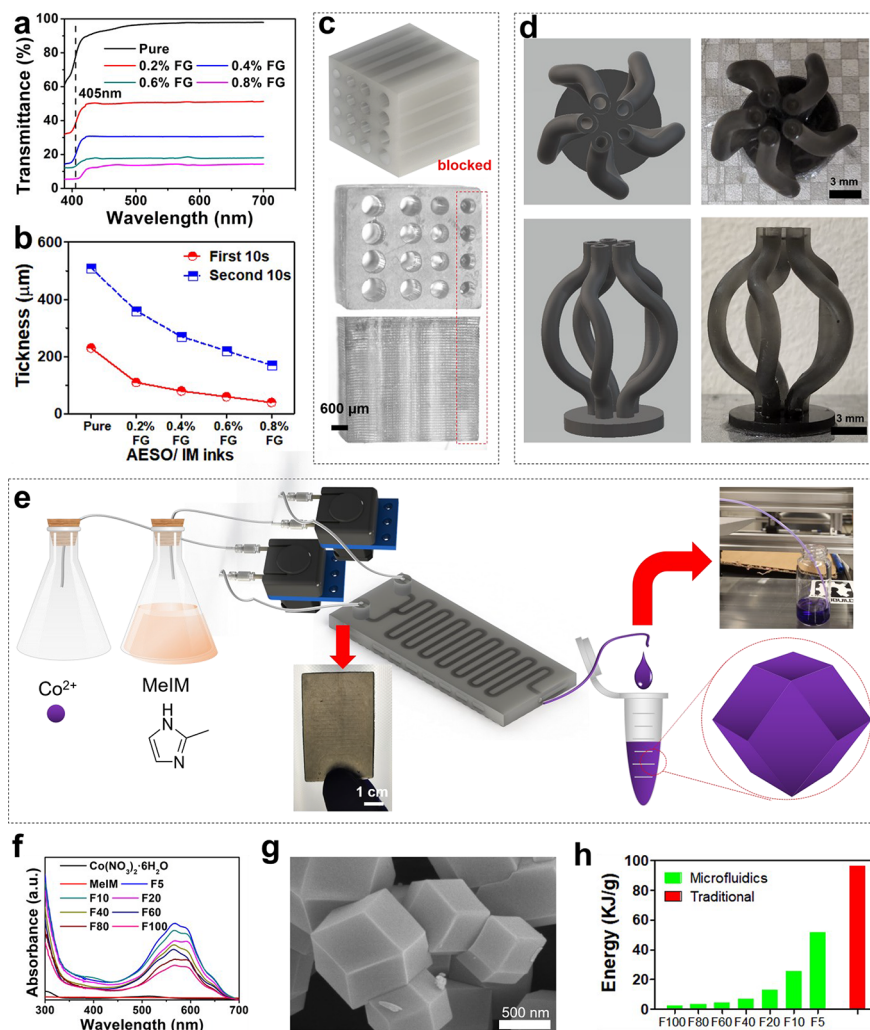


**Figure 4.** (a) Optical transmittances of printed AESO/IM biopolymer and AESO/IM/FG biocomposite with different FG weight ratios. They all have thicknesses of 2 mm. (b) Curing layer thickness of the inks with different FG weight ratios. (c) A CAD model and photographs of printed multiple layer microfluidic channels. (d) Photographs of CAD models and corresponding 3D-printed tubular structures. (e) Scheme of synthesizing ZIF-67 NPs by a 3D-printed microfluidic reactor. (f) UV-vis-NIR transmittance spectra of synthesized ZIF-67 NPs under various flow rates of precursors in the 3D-printed microfluidic channels. Rotation speeds of F5, F10, F20, F40, F60, F80, and F100 correspond to flow rates of 0.0425, 0.085, 0.17, 0.3225, 0.5, 0.6725, and 0.84 mL/min, respectively. (g) A SEM image of ZIF-67 NPs. (h) Specific energy consumption of synthesizing ZIF-67 NPs by a traditional batch reactor and a 3D-printed microfluidic reactor.

geometry, which can control sound absorption in a target frequency regime.<sup>27</sup> A 3D model of the acoustic metastructure with a lattice structure was designed and then printed (Figure 3e,f). The sound attenuation performance of the fabricated acoustic metastructure was tested in an impedance tube (Figure S7). It is noticed that the fabricated metamaterial possesses an extremely high absorption of sound starting from around ~3600 Hz, compared with the low-frequency absorption, peaked at ~2000 Hz of the solid structure (Figure 3g). The accuracy of the testing is also validated by conducting the sound absorption in the empty tube (Figure S8). It should be mentioned that this result shows that the acoustic absorption in a materials-saving lattice structure can be tuned and controlled by conducting optimization of the lattice structure. In summary, through topology optimization and structure design of an acoustic metastructure lattice, 3D printing of the biocomposite shows the advantage of reducing raw materials for sustainable applications.

#### The 3D-Printed Microfluidic Reactor for Nanomaterial Synthesis with Time Saving and Improved Efficiency.

FG can not only work as nanofillers to enhance the mechanical properties of the printed biocomposite objects but also act as a light absorption medium that prevents over-curing of the underlain layers when printing 3D tubular channels (FG changes the color of the ink from transparent to black). As shown in Figure 4a, the optical transmittance of the ink at 405 nm is greatly reduced with the increase of the FG weight ratio. As a result, the curing layer thickness decreases as the amount of FG increases (Figure 4b). It is <100 μm for the ink containing 0.6 wt % FG after the 10 s UV exposure. It increases with the increase of the exposure time. For instance, UV exposure of 20 s on the ink with 0.6 wt % FG results in the curing thickness of 220 μm. This overexposure may lead to blockage of underlain microchannels (Figure S9). Thus, we chose the printing parameters of 10 s light exposure and 100 μm of each layer thickness. To find out the printing resolution of microchannels, an array of microchannels was printed (Figure 4c). The smallest channel size that was achieved was <600 μm. With this information, we successfully printed 3D tubular microchannels (Figures 4d).

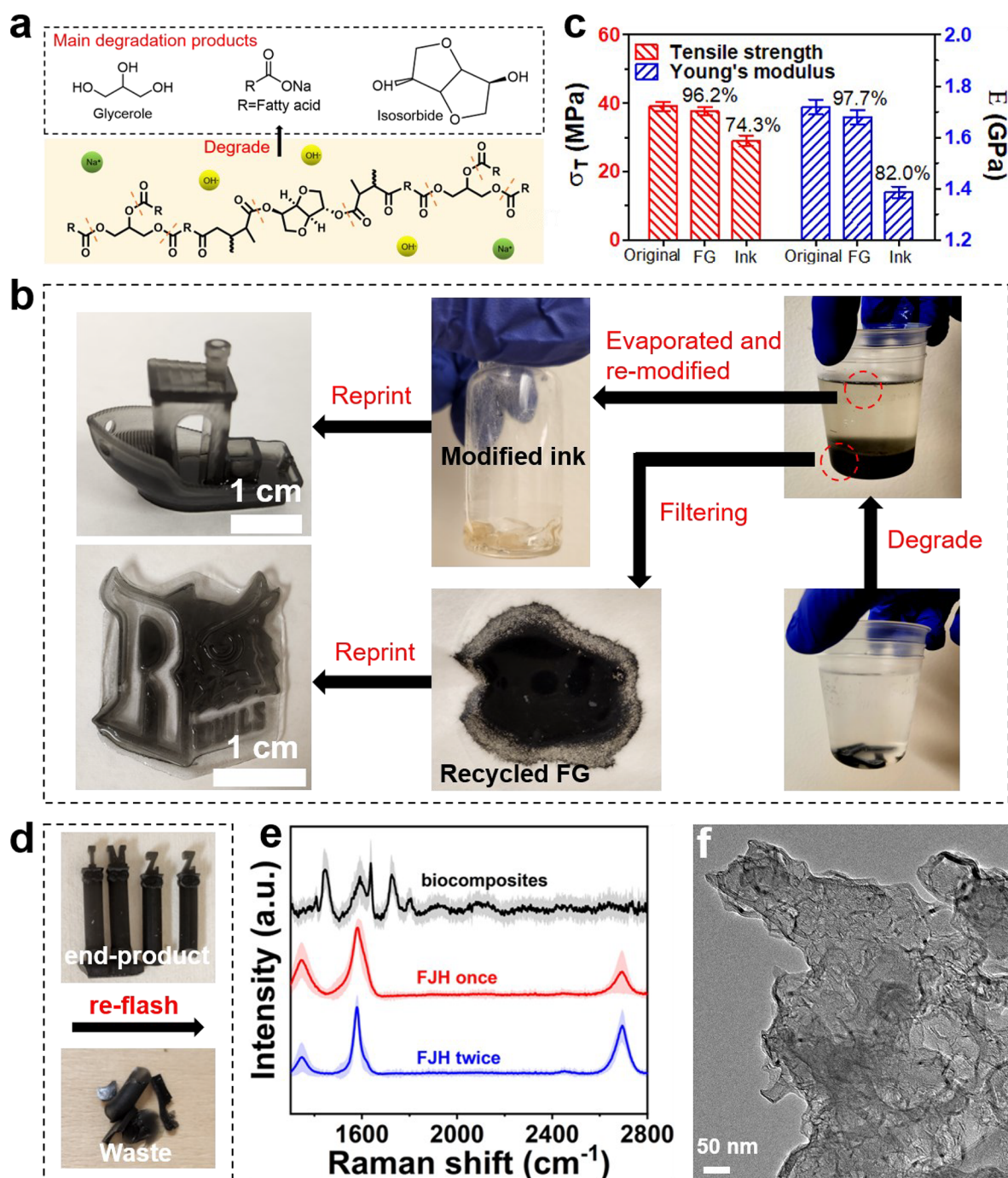


**Figure 5.** (a) Degradation mechanism and product of ASEO/IM biopolymer in alkaline aqueous solution. (b) Workflow of recycling FG and ink. (c) Tensile strength and Young's modulus of reprinted biocomposite with recycled FG and ink. (d) Photographs of end-products and waste biocomposite for FJH. (e) The average Raman spectra of biocomposite and FG after FJH of biocomposite once and twice, respectively. The standard deviation is shown as the shaded regions ( $N = 100$ ). (f) A TEM image of FG produced from FJH of a biocomposite.

A microfluidic reactor has the ability to promote biological and chemical reaction, separation, and detection in microchannels with sizes of hundreds of micrometers on a chip of several square centimeters.<sup>28</sup> Here, we assembled a printed microfluidic reactor for synthesis of zeolitic imidazolate framework (ZIF) nanoparticles (NPs), ZIF-67 (Figure 4e).<sup>29</sup> Despite various synthesis methods for ZIF or MOF synthesis, the widely deployed one is the batch synthesis one in a polytetrafluoroethylene autoclave. This traditional way of synthesizing ZIFs has disadvantages of low reactant and

energy usage efficiency. To demonstrate much improved efficiency in synthesizing ZIF-67 by the printed biocomposite microfluidic reactor, the reactants of cobaltous nitrate hexahydrate ( $\text{Co}(\text{NO}_3)_2 \cdot 6\text{H}_2\text{O}$ ) and 2-methylimidazole (MeIM) were pumped into the printed microchannels at accurately controlled flow rates (Video S1). Because of improved mass and energy transfer inside the microchannels, the reaction can be initiated at room temperature in a much more efficient way. Figure 4f shows the UV-vis spectra of the precursor solution and ZIF-67 NPs synthesized at different



flow rates ranging from 0.0425 to 0.84 mL/min. It is clearly observed that the mixture of  $\text{Co}^{2+}$  and MeIM led to the generation of  $[\text{Co}(\text{MeIM})_4]^{2+}$ , as demonstrated by the appearance of peaks within the range of 450 to 700 nm. In contrast, the spectra of both pure  $\text{Co}^{2+}$  and MeIM exhibit no peaks within the same range. Further observation reveals that a slower flow rate results in a higher peak intensity, indicating a higher concentration of  $[\text{Co}(\text{MeIM})_4]^{2+}$  due to a more efficient mixture of  $\text{Co}^{2+}$  and MeIM. These ZIF-67 NPs exhibit a dodecahedron shape with a sub-micrometer size (Figure 4g). When compared with the energy consumption resulting from a traditional hydrothermal reactor, there is 1.9–37.0 times reduction in the energy consumption of this microfluidic reactor at flow rates from 0.0425 to 0.84 mL/min (Figure 4h), which show a higher energy efficiency. Although the synthesis of ZIF-67 under room temperature is achievable,<sup>30,31</sup> the XRD results show that its crystallinity is a lot worse than that of ZIF-67 synthesized via the hydrothermal method and microfluidic one (Figure S10). Hence, in this work, we only compare the energy consumption by the microfluidic method with the hydrothermal one. In addition, the usage of both solvents and reactants in the printed microfluidic reactor can be significantly reduced compared with the hydrothermal method in the polytetrafluoroethylene autoclave due to their significantly different yields. The former one has a yield of 0.011 g/mL, while the later one has a yield of only 0.007 g/mL. Besides, the reaction in the microfluidic reactor can be continuous, as it can be operated under a continuous flow.

#### Recycling and Upgrading of Printed Biocomposite.

To show the ink recyclability, we degraded the biocomposite in a 3 wt % alkaline aqueous solution. The degradation is mainly caused by the hydrolysis of ester groups in the alkaline condition (Figure 5a). As a testing material, the printed biocomposite is made of A1-I3 and 0.6 wt % FG. After immersing in alkaline for 140 min it was completely degraded (Figures S11 and S12). The final products after degradation are the water-soluble glycerol, isosorbide, fatty acid salt and insoluble FG, which sank to the bottom of the bottle (Figure 5b). Then, FG can be filtered, washed, and recycled for reprinting of a new biocomposite. Figure 5c shows that the tensile strength and Young's modulus of the biocomposite using recycled FG were 97% and 98% of the ones of the original biocomposite, respectively. Meanwhile, the double bonds can be introduced to the hydrolysis product, i.e., isosorbide and glycerol through the esterification reaction (Figure S13).<sup>10,32</sup> The modified glycerol and isosorbide can be mixed with the resin of AESO and IM (A1-I3) for reprinting of new objects. The mass ratio of the recycled ink and the A1-I3 is 1 to 1, although the strength and modulus of the biocomposite printed by the recycled ink recover 74.3% and 82.0% (Figure 5c), respectively. The decrease in strength and modulus may be caused by the recycled impurities that do not participate in the cross-linking (i.e., fatty acid salt). Nevertheless, they still show a considerable tensile strength of 29.03 MPa and modulus of 1.38 GPa for some certain applications.

In addition to degrading the printed biocomposite for ink recycling, we can use the FJH process to upgrade end-of-use parts or wastes of printing to FG (Figure 5d). Figure S14 shows that after the pulsed voltage was applied twice, the conductivity of the FJH biocomposite was significantly improved, indicating its conversion to FG. The Raman spectra of the biocomposite after the first and second FJH show the

distinguished graphitic peaks with low defective density (Figure 5e). The FG yield of the FG is improved from 48% to 94% after FJH is applied twice (Table S3). Figure 5f shows the morphology of the FG produced from the biocomposite. Compared with FG produced from MC, the size of the FG produced from the biocomposite is statistically smaller (Figure S15). The profound  $2\theta$  peaks at  $26.5^\circ$  in the XRD spectra of the biocomposite after FJH was applied once and twice validate the conversion of the biocomposite to FG (Figure S16). The structure of the converted FG is turbostratic.<sup>16</sup> Thermogravimetric analysis (TGA) shows that the biocomposite degrades at  $\sim 240^\circ\text{C}$  (Figure S17), while the FG produced by FJH of the biocomposite has a thermal stability up to  $\sim 580^\circ\text{C}$ . XPS spectra show that carbon elements are dominant in the FG with an atomic percentage of  $\sim 95\%$  (Figure S18 and Table S4), indicating almost complete conversion. In this section, we can summarize that the components of the biocomposite ink can be recycled for reprinting, or the end-of-use and waste products can be upgraded for sustainability.

## CONCLUSIONS

In this work, sustainability in 3D printing was achieved by preparing a photocurable, degradable, renewable ink from a natural source, by recycling ink from the printed objects or upgrading the end-of-use biocomposite to FG, by demonstrating 3D printing of a biocomposite microfluidic reactor for synthesis of nanomaterials with time saving and improved energy efficiency. Moreover, we also demonstrate that FG can be deployed as the reinforcing nanofillers to strengthen the mechanical properties of the biocomposite as well as serving as a light absorber to improving the printing of the ink for fabricating 3D tubular microchannels. This work proves the success of the important aspects in sustainable 3D printing, which would inspire future exploration of the field.

## METHODS

**Materials.** 4-Dimethylaminopyridine (DMAP, >99%), methacrylic anhydride (MAA, >94%), and AESO were purchased from Sigma-Aldrich (St. Louis, MO, USA). Isosorbide (>98%), diphenyl(2,4,6-trimethylbenzoyl)phosphine oxide (TPO, >97%), and sodium bicarbonate were purchased from Fisher Scientific (Pittsburgh, PA, USA). These materials were used without further purification.

**Preparation of FG.** Metallurgical coke (MC) (5.7 g) was ground to various sizes before sieving. The portions with a mesh size of #12–20 underwent an FJH process at 370 V using a variable pulse with a duty cycle of 10% 1 s, 20% 0.5 s, and 50% 5 s to make FG. Further protocol and equipment specifics can be found in Chen et al.<sup>19</sup> The FG samples were then ball milled into powder for later use.

**Ink Preparation and Printing of the Biocomposite.** AESO and IM were mixed at various molar ratios of 1:1 (A1-I1), 1:2 (A1-I2), 1:3 (A1-I3), and 1:4 (A1-I4). The selected A1-I3 AESO-IM resin was mixed with 0.2 wt %, 0.4 wt %, 0.6 wt %, and 0.8 wt % FG. All the resins were added with a photoinitiator, diphenyl(2,4,6-trimethylbenzoyl)phosphine oxide (TPO) (2 wt %). The biocomposite was printed on an LCD printer (Anycubic Photon Mono X) with an irradiation wavelength of 405 nm under a power density of  $\sim 5\text{ mW/cm}^2$ . The thickness of each layer was set to 100  $\mu\text{m}$ , and the exposure time was set to 10 s. Then, the printed objects were post-cured by 405 nm UV light for 360 s.

**Degradation and Recycling of Biocomposites.** The printed biocomposite was immersed in a 3 wt % NaOH aqueous solution (300 mL) at  $80^\circ\text{C}$  for 140 min. The FG was recycled by filtration. The resulting isosorbide and glycerol are extracted by evaporation of degraded aqueous solution, then remodified by esterification to be



used as ink, and mixed with the original ink in a mass ratio of 1:1 for reprinting.

**FJH of the Biocomposite.** An electric hammer mill (DF-15 grinder) was used to completely pulverize the biocomposite sample. Then the biocomposite and MC were mixed at a 50–50 weight ratio. Two types of flashed samples were prepared, each with a mass of 560 mg. One sample was exposed to FJH by applying a 120 V pulse once, while the other was exposed to FJH by applying a 120 V pulse twice using a duty cycle of 10% 1 s, 20% 0.5 s, and 50% 5 s. Further protocol and equipment specifics can be found in Chen et al.<sup>19</sup>

**Synthesis of ZIF-67 NPs.** In the batch synthesis process by a polytetrafluoroethylene autoclave,  $\text{Co}(\text{NO}_3)_2 \cdot 6\text{H}_2\text{O}$  (1.092 g) and MeIM (2.464 g) were dissolved in 30 mL of MeOH to form two clear solutions, respectively. Then two solutions were mixed and stirred for 30 min and then transferred to a polytetrafluoroethylene autoclave (100 mL) and heated at 120 °C for 4 h. In the synthesis process using a microfluidic reactor,  $\text{Co}(\text{NO}_3)_2 \cdot 6\text{H}_2\text{O}$  (1.82 g) and MeIM (4.105 g) were dissolved in 50 mL of MeOH to form two clear solutions, respectively. Then two solutions were pumped into the microfluidic channels of 800  $\mu\text{m}$  in diameter, and a total of 14 turns were performed by two peristaltic pumps driven by stepper motors (BJ-RZ1030) under various rotation speeds of F5, F10, F20, F40, F60, F80, and F100, which correspond to flow rates of 0.0425, 0.085, 0.17, 0.3225, 0.5, 0.6725, and 0.84 mL/min, respectively. The operation was performed under room temperature. The energy consumption by the microfluidic reactor and the traditional hydrothermal reactor are both calculated by the equation  $W = UIt/m$ , where  $U$  is the working voltage,  $I$  is the working current,  $t$  is the working time, and  $m$  is the mass of synthesized ZIF-67 NPs. To simplify the calculation, we assumed a 100% energy conversion efficiency for both the hydrothermal reactor and the microfluidic reactor.

**Materials Characterization.** FTIR spectra were collected by a Thermo Nicolet 380 FTIR spectrometer with DIAMOND ATR. The viscosity of ink was evaluated by a modular rotation and interface rheometer MCR302 equipped with a C60/2°. The test was performed at room temperature with shear rates changing from 0.1 to 100 1/s. A Renishaw inVia Raman microscope outfitted with a 5 mW 532 nm laser was used to collect high-magnification spectra under a 50 $\times$  objective lenses. A Rigaku D/Max Ultima II Powder XRD 6s was used to collect the XRD patterns. A scan width of 0.05° per step and a scan rate of 0.5°/min were used to scan the samples in the range of 3° to 90°. A TA Instruments Q-600 TGA/DSC was used for TGA data collection in an air environment. The heating rate of 10 °C/min was applied to elevate the temperature until 780 °C. XPS spectra were collected by a PHI Quantera SXM scanning X-ray microprobe at a base pressure of  $5 \times 10^{-9}$  Torr. Survey spectra were recorded using a 0.5 eV step size at a pass energy of 140 eV. Elemental spectra were recorded using a 0.1 eV step size at a pass energy of 26 eV. All of the XPS spectra were corrected using the C 1s peaks (284.8 eV) as reference. TEM images were collected using a JEOL 2100F TEM system. The FG samples were sonicated in ethanol, then drop cast on lacy carbon grids and allowed to air-dry. An accelerating voltage of 200 kV was used for imaging. The optical images were obtained by an Amscope FMA050. The compression test was conducted on an MTS Landmark tensile tester. The tensile testing was conducted on a Mark-10 universal testing machine at a moving rate of 10 mm/min<sup>-1</sup>. Optical transmittance of ZIF-67 NPs was measured by a PerkinElmer Lambda 35 UV–vis spectrometer with an integrating sphere. Sound absorption test was measured by a microphone method via a Mecanum Inc. 1060-80 impedance tube. SEM images were collected using a ThermoScientific Volumescope at an accelerating voltage of 5.0 kV. The samples were coated with a thin gold film (8–10 nm) before imaging.

**Topology Optimization.** We adopted the formulation introduced by Giraldo-Londoño and Paulino for topology optimization of lightweight structures subjected to local stress constraints.<sup>25,26</sup> In a discretized setting, the objective is to find the material distribution, given by a design variable vector  $\mathbf{z} \in [0, 1]^N$ , where  $N$  is the number of elements in the finite element mesh such that the volume of the structure,  $f(\mathbf{z})$ , is minimized, while material failure constraints on the

form  $g_j(\mathbf{z}, \mathbf{u}) \leq 0$ ,  $j = 1, \dots, N$  are satisfied at the centroid of each finite element. Here,  $\mathbf{u} = \mathbf{K}^{-1}\mathbf{F}$  is the displacement vector, which is obtained via the finite element method. Formally, the topology optimization problem stated above is mathematically written as follows:

$$\begin{aligned} \min_{\mathbf{z} \in [0,1]^N} \quad & f(\mathbf{z}) = \frac{\mathbf{A}^T \mathbf{m}_V(\mathbf{y})}{\mathbf{A}^T \mathbf{1}} \\ \text{s. t.} \quad & g_l(\mathbf{z}, \mathbf{u}) \leq 0, \quad l = 1, \dots, N \\ \text{with} \quad & \mathbf{K}\mathbf{u} = \mathbf{F} \end{aligned} \quad (1)$$

where  $\mathbf{A} = \{\|\Omega_j\|\}_{j=1}^N$  is a vector containing the volume of each finite element in the mesh, and

$$m_V(y_l) = \frac{\tanh(\bar{\beta}\bar{\eta}) + \tanh(\bar{\beta}(y_l - \bar{\eta}))}{\tanh(\bar{\beta}\bar{\eta}) + \tanh(\bar{\beta}(1 - \bar{\eta}))} \quad (2)$$

represents the volume fraction of an element defined in terms of the threshold projection function.<sup>33</sup> Parameters  $\bar{\beta}$  and  $\bar{\eta}$  control the aggressiveness of the projection and the threshold projection density, respectively. Vector  $\mathbf{y} = \mathbf{P}\mathbf{z}$  contains the filtered densities for all elements in the mesh, where  $\mathbf{P}$  is the filter matrix given by

$$P_{ij} = \frac{w_{ij}A_j}{\sum_{k=1}^N w_{ik}A_k}, \quad \text{with } w_{ij} = \max\left(0, 1 - \frac{\|\mathbf{x}_i - \mathbf{x}_j\|_2}{R}\right)^q \quad (3)$$

where  $R$  is the filter radius and  $q$  is the nonlinear filter exponent.<sup>34</sup>

The stress constraints in eq 1 are based on the polynomial vanishing constraint:<sup>25</sup>

$$g_l(\mathbf{z}, \mathbf{u}) = m_E(y_l)\Lambda_l(\Lambda_l^2 + 1) \leq 0, \quad l = 1, \dots, N \quad (4)$$

where  $m_E(y_l) = \epsilon + (1 - \epsilon)m_V(y_l)^p$  is the SIMP interpolation function,<sup>35–37</sup> where  $\epsilon \ll 1$  and  $p$  is the SIMP penalization term. The unified failure function,  $\Lambda_l = \sigma_l^{\text{eq}} - 1$ , is expressed in terms of the equivalent stress measure:

$$\sigma_l^{\text{eq}} = \hat{\alpha}(\theta)\sqrt{3J_2} + \hat{\beta}I_1 + \hat{\gamma}I_1^2 \quad (5)$$

where  $\hat{\alpha}(\theta)$  is represented in eq 6:

$$\hat{\alpha}(\theta) = \frac{A \cos^2 \hat{\theta} + B}{C \cos \hat{\theta} + \sqrt{D \cos^2 \hat{\theta} + E}} \quad (6)$$

where  $\hat{\theta} = \frac{1}{3}\sin^{-1}(\zeta \sin 3\theta) + \bar{\theta}$  and  $\theta = \frac{1}{3}\sin^{-1}\left(-\frac{3\sqrt{3}J_3}{2J_2^{3/2}}\right)$  is the Lode

angle. The equivalent stress measure is written in terms of the first invariant of the Cauchy stress tensor,  $I_1$ , and the second and third invariants,  $J_2$  and  $J_3$ , of the deviatoric stress tensor, respectively, and parameters  $A$ ,  $B$ ,  $C$ ,  $D$ ,  $E$ ,  $\zeta$ ,  $\bar{\theta}$ ,  $\hat{\beta}$ , and  $\hat{\gamma}$ , which if chosen properly, can be used to represent several classical failure models including von Mises, Drucker-Prager, and Bresler-Pister, among others. In the present work, we adopt the Drucker-Prager criterion because it considers different strengths in tension and compression. The parameters reproducing the Drucker-Prager criterion are  $A = 0$ ,  $B = \frac{\sigma_c + \sigma_t}{2\alpha\sigma_t}$ ,  $C = 0$ ,  $D = 0$ ,  $E = 1$ ,  $\zeta = 1$ ,  $\bar{\theta} = 0$ ,  $\hat{\beta} = \frac{\sigma_c - \sigma_t}{2\alpha\sigma_t}$ , and  $\hat{\gamma} = 0$ , where  $\sigma_t$  and  $\sigma_c$  are the yield strength of the material obtained from uniaxial tension and uniaxial compression tests, respectively. Additional details of the formulation can be found in ref 25.

## ASSOCIATED CONTENT

### Supporting Information

The Supporting Information is available free of charge at <https://pubs.acs.org/doi/10.1021/acsnano.2c08157>.

Movie showing the synthesis of ZIF-67 by the printed biocomposite microfluidic reactor (MP4)

Photographs, TEM images, viscosity curves, reaction scheme, Raman spectra, XPS spectra, sound trans-

mission loss spectrum, mechanism of over-curing, weight loss curves, current response, XRD spectra, TGA curves, and summarized tables (PDF)

## AUTHOR INFORMATION

### Corresponding Authors

**James M. Tour** – Department of Chemistry, Department of Materials Science and NanoEngineering, and Department of Computer Science Engineering, NanoCarbon Center and the Welch Institute for Advanced Materials, Rice University, Houston, Texas 77005, United States; [orcid.org/0000-0002-8479-9328](https://orcid.org/0000-0002-8479-9328); Email: [tour@rice.edu](mailto:tour@rice.edu)

**Jian Lin** – Department of Mechanical and Aerospace Engineering, University of Missouri, Columbia, Missouri 65211, United States; [orcid.org/0000-0002-4675-2529](https://orcid.org/0000-0002-4675-2529); Email: [linjian@missouri.edu](mailto:linjian@missouri.edu)

### Authors

**Yuchao Wu** – Department of Mechanical and Aerospace Engineering, University of Missouri, Columbia, Missouri 65211, United States; [orcid.org/0000-0002-4221-1434](https://orcid.org/0000-0002-4221-1434)

**Paul A. Advincula** – Department of Chemistry, Rice University, Houston, Texas 77005, United States

**Oliver Giraldo-Londoño** – Department of Civil and Environmental Engineering, University of Missouri, Columbia, Missouri 65211, United States

**Yukai Yu** – Department of Mechanical and Aerospace Engineering, University of Missouri, Columbia, Missouri 65211, United States

**Yunchao Xie** – Department of Mechanical and Aerospace Engineering, University of Missouri, Columbia, Missouri 65211, United States

**Zhenru Chen** – Department of Mechanical and Aerospace Engineering, University of Missouri, Columbia, Missouri 65211, United States

**Guoliang Huang** – Department of Mechanical and Aerospace Engineering, University of Missouri, Columbia, Missouri 65211, United States

Complete contact information is available at:  
<https://pubs.acs.org/10.1021/acsnano.2c08157>

### Author Contributions

Y.W. and J.L. designed the project. Y.W., P.A.A., O.G.L., Y.Y., Y.X., and Z.C. performed the experiments and analyzed the results. G.H., J.M.T., and J.L. supervised the students performing the work and provided useful suggestions for this project. Y.W. and O.G.L. wrote the first draft, which was revised by J.L., G.H., and J.M.T. All other authors read and commented on the manuscripts.

### Notes

The authors declare no competing financial interest.

## ACKNOWLEDGMENTS

J.L. and J.M.T. thank the U.S. Army Corps of Engineers, ERDC (grant no. W912HZ-21-2-0050), for the financial support. J.M.T. also thanks the Air Force Office of Scientific Research (FA9550-19-0296) for support. O.G.L. acknowledges the endowment provided by the James W. and Joan M. O'Neill Faculty Scholar in Engineering at the University of Missouri. G.L.H. thanks the financial support from the U.S. Air Force Office of Scientific Research (grant no. AF 9550-20-0279) under Program Manager Dr. Byung-Lip (Les) Lee.

## REFERENCES

- (1) Gebler, M.; Schoot Uiterkamp, A. J. M.; Visser, C. A Global Sustainability Perspective on 3D Printing Technologies. *Energy Policy* **2014**, *74*, 158–167.
- (2) Ligon, S. C.; Liska, R.; Stampfl, J.; Gurr, M.; Mühlaupt, R. Polymers for 3D Printing and Customized Additive Manufacturing. *Chem. Rev.* **2017**, *117*, 10212–10290.
- (3) Wu, Y.; Fei, M.; Chen, T.; Li, C.; Wu, S.; Qiu, R.; Liu, W. Photocuring Three-Dimensional Printing of Thermoplastic Polymers Enabled by Hydrogen Bonds. *ACS Appl. Mater. Interfaces* **2021**, *13*, 22946–22954.
- (4) Wu, Y.; Fei, M.; Chen, T.; Li, C.; Fu, T.; Qiu, R.; Liu, W. H-bonds and Metal-Ligand Coordination-Enabled Manufacture of Palm Oil-Based Thermoplastic Elastomers by Photocuring 3D Printing. *Addit. Manuf.* **2021**, *47*, 102268.
- (5) Sanchez-Rexach, E.; Johnston, T. G.; Jehanno, C.; Sardon, H.; Nelson, A. Sustainable Materials and Chemical Processes for Additive Manufacturing. *Chem. Mater.* **2020**, *32*, 7105–7119.
- (6) Wu, Y.; Zeng, Y.; Chen, Y.; Li, C.; Qiu, R.; Liu, W. Photocurable 3D Printing of High Toughness and Self-Healing Hydrogels for Customized Wearable Flexible Sensors. *Adv. Funct. Mater.* **2021**, *31*, 2107202.
- (7) Gross, B. C.; Erkal, J. L.; Lockwood, S. Y.; Chen, C.; Spence, D. M. Evaluation of 3D Printing and Its Potential Impact on Biotechnology and the Chemical Sciences. *Anal. Chem.* **2014**, *86*, 3240–3253.
- (8) Sardon, H.; Mecerreyes, D.; Basterretxea, A.; Avérous, L.; Jehanno, C. From Lab to Market: Current Strategies for the Production of Biobased Polyols. *ACS Sustain. Chem. Eng.* **2021**, *9*, 10664–10677.
- (9) Guit, J.; Tavares, M. B. L.; Hul, J.; Ye, C.; Loos, K.; Jager, J.; Folkersma, R.; Voet, V. S. D. Photopolymer Resins with Biobased Methacrylates Based on Soybean Oil for Stereolithography. *ACS Applied Polymer Materials* **2020**, *2*, 949–957.
- (10) Liu, W.; Xie, T.; Qiu, R. Biobased Thermosets Prepared from Rigid Isosorbide and Flexible Soybean Oil Derivatives. *ACS Sustain. Chem. Eng.* **2017**, *5*, 774–783.
- (11) Zhou, J.; Xu, K.; Xie, M.; Wu, H.; Hua, Z.; Wang, Z. Two Strategies to Precisely Tune the Mechanical Properties of Plant Oil-Derived Epoxy Resins. *Compos. Part B. Eng.* **2019**, *173*, 106885.
- (12) Shin, Y.; Lim, Y.; Kwak, T.; Hwang, J. H.; Georgescu, A.; Huh, D.; Kim, D.; Kang, T. Microfluidic Multi-Scale Homogeneous Mixing with Uniform Residence Time Distribution for Rapid Production of Various Metal Core-Shell Nanoparticles. *Adv. Funct. Mater.* **2021**, *31*, 2007856.
- (13) Nasiri, R.; Shamloo, A.; Ahadian, S.; Amirifar, L.; Akbari, J.; Goudie, M. J.; Lee, K.; Ashammakhi, N.; Dokmeci, M. R.; Di Carlo, D.; Khademhosseini, A. Microfluidic-Based Approaches in Targeted Cell/Particle Separation Based on Physical Properties: Fundamentals and Applications. *Small* **2020**, *16*, 2000171.
- (14) Xu, Y.; Qi, F.; Mao, H.; Li, S.; Zhu, Y.; Gong, J.; Wang, L.; Malmstadt, N.; Chen, Y. In-Situ Transfer Vat Photopolymerization for Transparent Microfluidic Device Fabrication. *Nat. Commun.* **2022**, *13*, 918.
- (15) Grigoryan, B.; Paulsen, S. J.; Corbett, D. C.; Sazer, D. W.; Fortin, C. L.; Zaita, A. J.; Greenfield, P. T.; Calafat, N. J.; Gounley, J. P.; Ta, A. H.; Johansson, F.; Randles, A.; Rosenkrantz, J. E.; Louis-Rosenberg, J. D.; Galie, P. A.; Stevens, K. R.; Miller, J. S. Multivascular Networks and Functional Intravascular Topologies within Biocompatible Hydrogels. *Science* **2019**, *364*, 458–464.
- (16) Luong, D. X.; Bets, K. V.; Algozeeb, W. A.; Stanford, M. G.; Kittrell, C.; Chen, W.; Salvatierra, R. V.; Ren, M.; McHugh, E. A.; Advincula, P. A.; Wang, Z.; Bhatt, M.; Guo, H.; Mancevski, V.; Shahsavari, R.; Yakobson, B. I.; Tour, J. M. Gram-Scale Bottom-Up Flash Graphene Synthesis. *Nature* **2020**, *577*, 647–651.
- (17) Algozeeb, W. A.; Savas, P. E.; Luong, D. X.; Chen, W.; Kittrell, C.; Bhat, M.; Shahsavari, R.; Tour, J. M. Flash Graphene from Plastic Waste. *ACS Nano* **2020**, *14*, 15595–15604.

- (18) Wyss, K. M.; De Kleine, R. D.; Couvreur, R. L.; Kiziltas, A.; Mielewski, D. F.; Tour, J. M. Upcycling End-Of-Life Vehicle Waste Plastic into Flash Graphene. *Commun. Eng.* **2022**, *1*, 3.
- (19) Chen, W.; Ge, C.; Li, J. T.; Beckham, J. L.; Yuan, Z.; Wyss, K. M.; Advincula, P. A.; Eddy, L.; Kittrell, C.; Chen, J.; Luong, D. X.; Carter, R. A.; Tour, J. M. Heteroatom-Doped Flash Graphene. *ACS Nano* **2022**, *16*, 6646–6656.
- (20) Zhu, G.; Zhang, J.; Huang, J.; Yu, X.; Cheng, J.; Shang, Q.; Hu, Y.; Liu, C.; Hu, L.; Zhou, Y. High-Performance 3D Printing UV-Curable Resins Derived from Soybean Oil and Gallic Acid. *Green Chem.* **2021**, *23*, 5911–5923.
- (21) Ma, S.; Jiang, Y.; Liu, X.; Fan, L.; Zhu, J. Bio-based Tetrafunctional Crosslink Agent from Gallic Acid and its Enhanced Soybean Oil-Based UV-Cured Coatings with High Performance. *RSC Adv.* **2014**, *4*, 23036–23042.
- (22) Wang, B.-T.; Lu, F.-D.; Xu, F.; Li, Y.-Z.; Kessler, M. R. Synthesis of Renewable Isosorbide-Based Monomer and Preparation of the Corresponding Thermosets. *Chin. Chem. Lett.* **2016**, *27*, 875–878.
- (23) Schimpf, V.; Asmacher, A.; Fuchs, A.; Bruchmann, B.; Mülhaupt, R. Polyfunctional Acrylic Non-isocyanate Hydroxyurethanes as Photocurable Thermosets for 3D Printing. *Macromolecules* **2019**, *52*, 3288–3297.
- (24) Bendsoe, M. P.; Kikuchi, N. Generating Optimal Topologies in Structural Design Using a Homogenization Method. *Comput. Methods Appl. Mech. Eng.* **1988**, *71*, 197–224.
- (25) Giraldo-Londoño, O. G.; Paulino, H. A Unified Approach for Topology Optimization with Local Stress Constraints Considering Various Failure Criteria: Von Mises, Drucker-Prager, Tresca, Mohr-Coulomb, Bresler-Pister and Willam-Warnke. *P. R. Soc. A* **2020**, *476*, 20190861.
- (26) Sasaki, M.; Itō, T.; Isozaki, A. *Morphogenesis of flux structure*; Aa Publications: 2007.
- (27) Yu, K.; Fang, N. X.; Huang, G.; Wang, Q. Magnetoactive Acoustic Metamaterials. *Adv. Mater.* **2018**, *30*, 1706348.
- (28) Su, R.; Wen, J.; Su, Q.; Wiederoder, M. S.; Koester, S. J.; Uzarski, J. R.; McAlpine, M. C. 3D Printed Self-Supporting Elastomeric Structures for Multifunctional Microfluidics. *Sci. Adv.* **2020**, *6*, eabc9846.
- (29) Pan, Y.; Sun, K.; Liu, S.; Cao, X.; Wu, K.; Cheong, W.-C.; Chen, Z.; Wang, Y.; Li, Y.; Liu, Y.; Wang, D.; Peng, Q.; Chen, C.; Li, Y. Core-Shell ZIF-8@ZIF-67-Derived CoP Nanoparticle-Embedded N-Doped Carbon Nanotube Hollow Polyhedron for Efficient Overall Water Splitting. *J. Am. Chem. Soc.* **2018**, *140*, 2610–2618.
- (30) Kuruppathparambil, R. R.; Jose, T.; Babu, R.; Hwang, G.; Kathalikkattil, A. C.; Kim, D.; Park, D. A Room Temperature Synthesizable and Environmental Friendly Heterogeneous ZIF-67 Catalyst for the Solvent Less and Co-Catalyst Free Synthesis of Cyclic Carbonates. *Appl. Catal. B: Environ.* **2016**, *182*, 562–569.
- (31) Wang, H.; Xie, Y.; Li, D.; Deng, H.; Zhao, Y.; Xin, M.; Lin, J. Rapid Identification of X-Ray Diffraction Patterns Based on Very Limited Data by Interpretable Convolutional Neural Networks. *J. Chem. Inf. Model.* **2020**, *60*, 2004–2011.
- (32) Fei, M.; Liu, T.; Fu, T.; Zhang, J.; Wu, Y.; Qiu, R.; Liu, W. Styrene-Free Soybean Oil Thermoset Composites Reinforced by Hybrid Fibers from Recycled and Natural Resources. *ACS Sustain. Chem. Eng.* **2019**, *7*, 17808–17816.
- (33) Wang, F.; Lazarov, B. S.; Sigmund, O. On Projection Methods, Convergence and Robust Formulations in Topology Optimization. *Struct. Multidiscipl. Optim.* **2011**, *43*, 767–784.
- (34) Zegard, T.; Paulino, G. H. Bridging Topology Optimization and Additive Manufacturing. *Struct. Multidiscipl. Optim.* **2016**, *53*, 175–192.
- (35) Bendsoe, M. P. Optimal Shape Design as a Material Distribution Problem. *Struct. Optim.* **1989**, *1*, 193–202.
- (36) Zhou, M.; Rozvany, G. I. N. The COC algorithm, Part II: Topological, Geometrical and Generalized Shape Optimization. *Comput. Methods Appl. Mech. Eng.* **1991**, *89*, 309–336.
- (37) Rozvany, G. I. N.; Zhou, M.; Birker, T. Generalized Shape Optimization without Homogenization. *Struct. Optim.* **1992**, *4*, 250–252.